J. Fluid Mech. (2006), *vol.* 547, *pp.* 413–441. © 2006 Cambridge University Press
doi:10.1017/S0022112005007342 Printed in the United Kingdom

Numerical simulations of boundary-layer transition induced by a cylinder wake

By VICTOR OVCHINNIKOV[1], UGO PIOMELLI[1] AND MEELAN M. CHOUDHARI[2]

[1]Department of Mechanical Engineering, University of Maryland, College Park, MD 20742, USA
[2]NASA Langley Research Center, Hampton, VA 23681, USA

(Received 28 December 2004 and in revised form 20 July 2005)

Direct and large-eddy simulations of the interaction between a laminar boundary layer and a von Kármán vortex street behind a circular cylinder are carried out for three values of the Reynolds number based on the cylinder diameter and free-stream velocity: $Re_D = 385$, 1155 and 3900. Rapid, bypass-like transition to turbulence is observed in the two higher-Reynolds-number cases. Flow statistics in the transitional and turbulent regions are examined, followed by an investigation of the underlying transition mechanism. Qualitative similarities between wake-induced transition and bypass transition due to free-stream turbulence are discussed and the challenges of predicting boundary-layer transition in this complex environment are pointed out.

1. Introduction

High-lift systems have a significant impact on the overall cost and safety of aircraft. According to Meredith (1993), a 1 % improvement in the maximum lift coefficient (or lift-to-drag ratio) could translate into an increased payload of 14 to 22 passengers on a large twin-engine transport airplane. An optimal aerodynamic design of a multi-airfoil high-lift configuration requires careful consideration of both inviscid and viscous flow phenomena. In particular, laminar-to-turbulent transition is a crucial issue for ground-to-flight scaling of high-lift flow fields.

The familiar transition mechanisms over a single isolated airfoil are also relevant to transition over the multi-element airfoil configurations encountered in high-lift applications. These include, respectively, transition due to one or more types of hydrodynamic instabilities (attachment line instabilities, streamwise instabilities in the form of Tollmien–Schlichting waves or Rayleigh modes, and crossflow vortex instabilities) or leading-edge contamination – a form of subcritical (i.e. bypass) transition. An additional transition mechanism that is unique to multi-element airfoils involves boundary-layer contamination due to unsteady wakes of upstream elements or additional types of vortical disturbances originating from the separated cove flow beneath an upstream element. While the 'single-element' class of transition mechanisms has been widely studied in the literature (see, for example, Kusunose & Cao 1994), the wake-contamination issue has received little scrutiny thus far and is the focus of this paper. Transition due to wake/boundary-layer interaction is also known to occur in turbine flows, where the interaction involves the wake of an upstream blade and the boundary layer of a downstream one. The transition process in this case is inherently unsteady. As the wake impinges on the downstream airfoil, a turbulent region analogous to a turbulent spot is formed locally, which travels in

https://doi.org/10.1017/S0022112005007342 Published online by Cambridge University Press

the boundary layer of the downstream blade and perturbs it. Wake/boundary-layer interaction over multi-element airfoils involves the wake of an upstream element that develops nearly parallel to the boundary layer on a downstream one. Wake-induced transition in this case is due to a steady interaction in which the position of the wake and the resulting onset of transition remain fixed with respect to the boundary layer.

Most of the prior investigations of the interactions between turbulent wakes and boundary layers have concentrated on the unsteady case. The unsteady character of the impingement zone (which travels downstream in time) plays an important role in the dynamics of the flow, as shown by a number of investigators (see, for example, Liu & Rodi 1991; Wu *et al.* 1999, and references therein). In contrast, the number of studies devoted to steady wake/boundary-layer interactions is much smaller. Squire (1989) summarizes many of the investigations conducted prior to 1989. Particularly important is the work by Zhou & Squire (1985), who examined the interaction between the wake of an airfoil and a flat plate. They found that a region in which the wake and boundary layer are separated by a potential core is followed by a merging zone. Across this zone, the velocity profile in the outer part of the boundary layer is substantially different from that in a regular flat-plate boundary layer. Zhou & Squire also observed that the positions of zero Reynolds shear stress and zero mean velocity gradient do not coincide, indicating that the Boussinesq approximation inherent in the scalar eddy-viscosity models becomes suspect in such flows.

Kyriakides *et al.* (1996) performed experiments on boundary-layer transition induced by a von Kármán vortex street behind a circular cylinder. The cylinder was mounted above the plate, and the Reynolds number based on cylinder diameter was varied between 385 and 10 500. These authors reported transition for all Reynolds numbers and noted several interesting trends as the diameter of the cylinder and its location relative to the plate were varied. Unfortunately, their paper did not contain turbulent statistics besides profiles of the mean streamwise velocity and disturbance spectra at their lowest Reynolds number. More importantly from our standpoint, the transitional aspects of the boundary-layer flow were not investigated in detail.

In most wake/boundary-layer interaction scenarios, the wake is initially separated from the boundary layer and merges with it some distance downstream. The merging distance depends, of course, on the spreading rate of the wake and on the boundary-layer growth (i.e. on the Reynolds number), as well as on the initial distance between the wake and the solid body. The shape of the body that forms the wake is also important: bluff-body wakes are characterized by a von Kármán vortex street that involves strong coherent eddies (the spanwise 'rollers'), along with 'braid vortices' between the rollers. Wakes of airfoils or flat plates may or may not contain such coherent motions, depending, among other factors, on the sharpness of the trailing edge, on whether the flow is attached or separated, etc. In the case of bluff-body wakes, two types of interaction can be identified (Zhou & Squire 1985): a 'strong interaction' case that occurs when the wake still contains coherent eddies in the interaction region, and a 'weak interaction' case, in which the interaction takes place sufficiently far downstream of the cylinder that the spanwise rollers have decayed.

The present paper will focus on a numerical simulation of two element transition scenarios in the simplified case of a cylinder placed above the leading edge of a flat plate; boundary-layer transition is induced by the wake generated by the cylinder (see figure 1). Because of the extensive prior studies pertaining to flat-plate and cylinder flows in isolation, the cylinder–plate combination is convenient yet retains the essential physics of realistic complex geometry cases. Furthermore, the experimental data of Kyriakides *et al.* (1996) can be used to validate some of the computational results.

https://doi.org/10.1017/S0022112005007342 Published online by Cambridge University Press

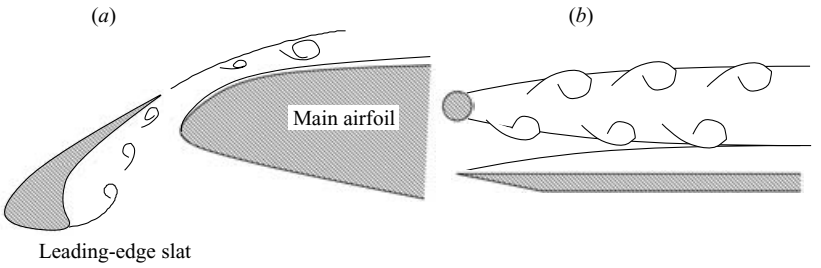


FIGURE 1. Sketch of (*a*) the multi-airfoil configuration and (*b*) the model problem.

Kyriakides *et al.* discussed two of the cases simulated here, namely $Re_D = 385$ and $Re_D = 1155$ (cases 1 and 2 in their paper). They also report a case at $Re_D = 3500$, close to the $Re_D = 3900$ case studied herein.

The streamwise location of the cylinder axis is taken to be directly above the leading edge of the flat plate. Our simulations begin upstream of the cylinder and the flat plate leading edge and extend into the fully turbulent region, thus including the entire domain of interest.

The present paper is organized as follows. First we present the numerical formulation, details of the configuration geometry, and the initial and boundary conditions. We then discuss flow validation and resolution studies. Next, we show and discuss the results, with an emphasis on the transition mechanism and transition prediction. We end with possible directions for future investigations.

2. Problem formulation

In the present study, we perform both direct and large-eddy simulations of incompressible flow. In the case of direct numerical simulations (DNS), we solve the incompressible equations of conservation of mass and momentum:

$$\frac{\partial u_j}{\partial x_j} = 0, \tag{2.1}$$

$$\frac{\partial u_i}{\partial t} + \frac{\partial}{\partial x_j}(u_j u_i) = -\frac{1}{\rho}\frac{\partial p}{\partial x_i} + \frac{1}{Re_D}\nabla^2 u_i + f_i, \tag{2.2}$$

while in the case of the large-eddy simulation (LES), we use the filtered equations of motion:

$$\frac{\partial \overline{u}_j}{\partial x_j} = 0, \tag{2.3}$$

$$\frac{\partial \overline{u}_i}{\partial t} + \frac{\partial}{\partial x_j}(\overline{u}_j \overline{u}_i) = -\frac{1}{\rho}\frac{\partial \overline{p}}{\partial x_i} + \frac{1}{Re_D}\nabla^2 \overline{u}_i - \frac{\partial \tau_{ij}}{\partial x_j} + \overline{f_i}, \tag{2.4}$$

where the overbar represents the filtered variables, and $\tau_{ij} = \overline{u_i u_j} - \overline{u}_i \overline{u}_j$ is the subgrid-scale stress (SGS), which in the present calculations was modelled using the dynamic eddy-viscosity model with Lagrangian averaging (Meneveau, Lund & Cabot 1996). The equations above have been made dimensionless using the free-stream velocity U_∞ and the cylinder diameter D. The resulting Reynolds number is defined as $Re_D = U_\infty D/\nu$. The presence of the body forces f_i is due to the immersed boundary method, described below.

The equations of motion are solved using a fractional step method (Chorin 1968; Kim & Moin 1985). We use a staggered-grid arrangement, with central approximations

https://doi.org/10.1017/S0022112005007342 Published online by Cambridge University Press

for all the derivatives and explicit Adams–Bashforth time advancement for the convective and diffusive terms. The method is second-order accurate in both time and space. Following the time advancement step, the predicted velocity field is made solenoidal by solving the Poisson equation for the pseudo-pressure and correcting the predicted velocities with the pseudo-pressure gradient. The method fully conserves mass, momentum and energy in the discrete sense (see Morinishi *et al*. 1998). The coordinates x_1, x_2 and x_3 (or, interchangeably, x, y and z) refer, respectively, to the streamwise, wall-normal and spanwise velocity directions. The grid is uniform in the spanwise direction and stretched in the streamwise and wall-normal directions to ensure adequate resolution within the boundary layer (particularly in the transitional region) and the convecting cylinder wake. The code has been extensively validated for a variety of turbulent and relaminarizing flows (Balaras, Benocci & Piomelli 1995; Piomelli, Balaras & Pascarelli 2000; Balaras, Piomelli & Wallace 2001).

The above algorithm was parallelized using the message-passing interface (MPI). The computational box is divided into n equal subdomains in the flow direction and each of the n processors integrates the equations of motion in one of the subdomains. The pseudo-pressure field is obtained by applying a spanwise fast Fourier transform (FFT) to the discrete Poisson equation. This yields a pentadiagonal matrix for each Fourier mode, which is then inverted by a cyclic reduction algorithm. Each processor is assigned a subset of the Fourier modes resulting from the application of FFT.

The Cartesian computational grid does not conform to the cylinder body. To satisfy the no-slip boundary conditions at the cylinder surface, we employ the immersed boundary method of Fadlun *et al.* (2000), following the implementation of Balaras (2004). In this procedure, the body forces f_i or $\overline{f}_i$ are non-zero only in grid cells near the cylinder surface and are assigned in such a way that the velocity on the cylinder surface is zero to second-order. When the predicted velocity is projected onto a divergence-free field, the velocity perturbations that are introduced in the vicinity of the cylinder are small (Fadlun *et al.* 2000), so that the corrected velocity is also second-order accurate around the cylinder body. Finally, we note that in the case of explicit time advancement, calculating and including a force field in the momentum equations is equivalent to modifying the predicted velocities directly. The immersed boundary method, as described above, has been extensively validated in laminar and turbulent flows in the references mentioned above. For further validation in the specific context of interest, we also performed an LES of the flow past a circular cylinder at $Re_D = 3900$, which will be described in § 3.

2.1. *Initial and boundary conditions*

Figure 2 shows a sketch of the computational configuration and boundary conditions. All our calculations start ten cylinder diameters upstream of the flat-plate leading edge. On the lower side of the domain, ahead of the leading edge of the plate, we apply free-slip conditions ($\partial u/\partial y = \partial w/\partial y = 0$, $v = 0$), and no-slip conditions on the plate. In order to avoid the numerical difficulties associated with modelling a sharp leading edge (i.e. the possibility of numerical instabilities due to the sudden change from the homogeneous Neumann to the Dirichlet conditions), we merged the two conditions smoothly over a length $x \simeq 8$ using a hyperbolic tangent function. Since the flow around the leading edge is slowed down gradually rather than suddenly, the above merging amounts to modelling a finite-thickness leading edge. We verified that the mean velocity profiles sufficiently far downstream of the leading edge asymptote to the Blasius solution.

https://doi.org/10.1017/S0022112005007342 Published online by Cambridge University Press

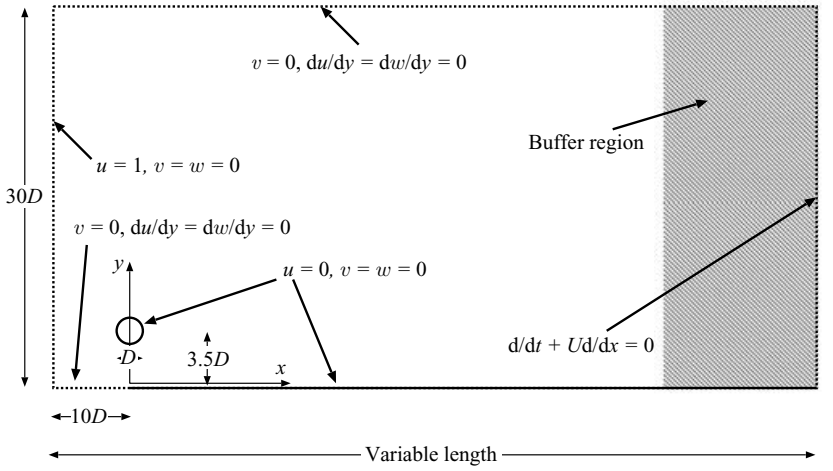


FIGURE 2. Computational configuration and boundary conditions.

Along the free-stream boundary, we imposed free-slip conditions. This boundary condition does not allow outflow through the top side of the domain, causing the flow above the boundary layer to accelerate in order to compensate for the boundary-layer growth. In our simulations, the acceleration parameter due to this effect, $K \equiv -(\nu/U_\infty^2)(\mathrm{d}U_\infty/\mathrm{d}x)$, was of the order of 10^{-7}. The value of K at which a turbulent boundary layer is expected to relaminarize is around 3.0×10^{-6} (Spalart 1986). Since in our case, K is an order of magnitude lower, we do not expect the acceleration to affect transition significantly.

The inlet condition consisted of a uniform streamwise velocity profile. At the outflow, we imposed non-reflecting boundary conditions (Orlanski 1976). Simulation results in the last 15 % of the domain were discarded because of the proximity of the outflow boundary. Since the grid was stretched significantly in this region, however, only about 7 % of the grid cells were wasted. In the spanwise direction, z, periodic boundary conditions were used.

The three calculations performed in this work required substantial computational resources, especially those at $Re_D = 1155$ and $Re_D = 3900$. The computational expense was necessary to resolve properly the boundary-layer leading edge, the cylinder wake, and the transitional region of the boundary layer, which is known to be sensitive to the grid resolution (Jacobs & Durbin 2001; Ovchinnikov, Piomelli & Choudhari 2004). Therefore, two overlapping computational domains were used in the above two cases to minimize the computational resources required. The first box contained the cylinder and the flat-plate leading edge and had very fine resolution near the wall and near the cylinder surface (to allow accurate implementation of the immersed boundary method) as well as in the shear layers emanating from the cylinder separation. Some distance downstream of the cylinder, where the boundary layer is thicker and the smallest scales within the cylinder wake have grown substantially, the wall-normal resolution requirement could be relaxed. At this location, a time sequence of planes of velocity was stored and used as the inflow condition for a second computational domain that had fewer points in the wall-normal direction, but maintained the fine streamwise resolution required to resolve the transition zone (Jacobs & Durbin 2001; Ovchinnikov *et al.* 2004). The multi domain aproach has been used successfully in the

https://doi.org/10.1017/S0022112005007342 Published online by Cambridge University Press

Case	Re	Method	$L_x \times L_y \times L_z$	$nx \times ny \times nz$
1	385	DNS	$150 \times 20 \times 2\pi$ $100 \times 20 \times 2\pi$ (useful)	$1128 \times 192 \times 48$
2	1155	LES	$100 \times 20 \times 2\pi$ (box 1) $115 \times 20 \times 2\pi$ (box 2) $160 \times 20 \times 2\pi$ (useful)	$1056 \times 384 \times 128$ (box 1) $624 \times 200 \times 128$ (box 2)
3	3900	DNS	$30 \times 20 \times 2\pi$ (box 1) $60 \times 20 \times 2\pi$ (box 2) $58 \times 20 \times 2\pi$ (useful)	$608 \times 448 \times 160$ (box 1) $1168 \times 310 \times 160$ (box 2)

TABLE 1. Simulation parameters.

past (Rai & Moin 1993; Huai, Joslin & Piomelli 1997). However, strictly speaking, it violates the ellipticity of the incompressible Navier–Stokes (NS) equations. To estimate the magnitude of the errors, we performed two DNS of the flow past a circular cylinder at $Re_D = 3900$. In the first, the computational domain was inside a single box spanning $x = -10D$–$8D$, and in the second, it was split between two boxes spanning $x = -10D$–$4.7D$ and $x = 4.7D$–$8D$, respectively. The cylinder axis was located at $(x, y) = (0D, 15D)$ and the wall-normal domain was $30D$. The wall-normal domain had 352 cells in the first simulation and the first box of the second simulation, and 232 cells in the second box of the second simulation. Linear interpolation was used to transfer the velocity from the outflow plane of the first box to the inflow plane of the second box. The resolution was in accordance with the validation study presented in the next section. The simulations were started from the same initial field and advanced synchronously. This permitted comparisons of instantaneous as well as time-averaged fields. For the two simulations, contours of the instantaneous velocity were almost indistinguishable in the region $x = 4.7D$–$8D$. The maximum deviation in the mean velocity in this region was 4 %, and the streamwise Reynolds stress $\langle uu \rangle$ was underpredicted by at most 8 % in the two-box simulation. This mild underprediction is expected since linear interpolation used to transfer the velocity field is dissipative. Overall, the error incurred by the multi domain approach is justified by 34 % savings in computational time.

Despite the reduced cost of the approach, the simulations required a total of 65 and 80 million points for the $Re_D = 1155$ and $Re_D = 3900$ cases, respectively. In order to obtain converged statistics, each case required a total CPU time of 300–400 hours per processor on an 8-processor Pentium 4 cluster.

The initial condition for the low-Reynolds-number calculation ($Re_D = 385$) was a uniform velocity profile throughout the entire domain. For the first box of the higher-Reynolds-number calculations, the initial condition was obtained by interpolating the converged velocity field from a lower-Reynolds-number calculation. For the second box, a Blasius boundary-layer solution with the appropriate boundary-layer thickness at the inlet (obtained from the first box) was used as initial condition.

2.2. *Simulation parameters*

The flat-plate leading edge was located at $x = 10$ on the bottom boundary, and the cylinder axis at $x = 10$, $y = 3.5$ for all simulations (as mentioned above, all lengths are made dimensionless by the cylinder diameter D), as shown in figure 2. Table 1 summarizes the simulation parameters. The computational domain for the $Re_D = 385$ case was a rectangular box of dimensions $L_x \times L_y \times L_z = 150 \times 20 \times 2\pi$. For the

https://doi.org/10.1017/S0022112005007342 Published online by Cambridge University Press

Method	*Re*	Δx^+_{max}	Δy^+_{max}	Δz^+_{max}
DNS	385	7.0	0.25	3.0
LES	1155 (box 1)	10.0	0.21	2.8
LES	1155 (box 2)	12.0	1.0	3.1
DNS	3900 (box 1)	4.0	0.3	6.0
DNS	3900 (box 2)	10.5	0.9	7.0

TABLE 2. Largest grid size in viscous units ($\Delta^+(x) = \Delta(x)u_\tau(x)/\nu$) near the flat plate.

$Re_D = 1155$ case, the first box had dimensions $100 \times 20 \times 2\pi$; cross-stream planes were extracted at location $x = 60$, interpolated onto the wall-normal mesh of box 2, and fed into a second computational box of dimensions $115 \times 20 \times 2\pi$. With respect to the flat-plate leading edge, the useful region of the calculation, therefore, extended from $x = -10$ to $x = 150$ (the last 15 units of the second domain are discarded because the grid stretching results in excessive coarseness of the mesh in this region, and the effect of the outflow boundary conditions alters the flow physics). For the $Re_D = 3900$ case, the first box had dimensions $30 \times 20 \times 2\pi$; cross-stream planes were extracted at $x = 17.3$ and fed into a second box of dimensions $60 \times 20 \times 2\pi$. For the highest-Reynolds-number simulation, the computational domain could be short because transition takes place closer to the leading edge than in the other cases. As will be shown, in the $Re_D = 1155$ case, transition begins in the first box and completes in the second box, while in the $Re_D = 3900$ case, the transition process is entirely confined to the second box.

The governing equations were advanced in time until a steady state was reached, statistics were then accumulated for a period of 150 in dimensionless units. Convergence of the statistical sample was verified by comparing the statistics obtained using only half of the sample with those obtained using the entire sample. First-order quantities differed by less than 1 %, second moments by less than 5 %.

3. Grid requirements

In order to ensure the accuracy of our calculations, we had to establish separate grid resolution requirements for the evolving boundary layer and the cylinder wake. The grid requirements for the simulation of turbulent boundary layers using second-order accurate schemes are well known ($\Delta x^+ \simeq 15$, $\Delta y^+_{min} < 1$, $\Delta z^+ \simeq 6$ for DNS, $\Delta x^+ \simeq 50$, $\Delta y^+_{min} < 1$, $\Delta z^+ \simeq 20$ for LES) and were easily achieved in the fully turbulent region. Table 2 shows the largest grid size in wall units for all the calculations.

For transitional flows, the grid requirements are less well established. However, the results presented in this paper will show that the phenomenon of wake-induced transition is analogous to bypass transition due to free-stream turbulence (f.s.t.). Accordingly, the computational grids used in the present study were based on previous work related to f.s.t. induced transition (see Jacobs & Durbin 2001; Ovchinnikov *et al.* 2004). As argued in these references, boundary-layer bypass transition is especially sensitive to streamwise resolution. Ovchinnikov *et al.* (2004) show that an excessively coarse streamwise grid compromises the evolution of the turbulence spots characteristic of boundary-layer bypass transition (Jacobs & Durbin 2001; Brandt, Schlatter & Henningson 2004; Ovchinnikov *et al.* 2004), and that under-resolved calculations predict a premature and abrupt transition. In all of our simulations, the

https://doi.org/10.1017/S0022112005007342 Published online by Cambridge University Press

streamwise grid spacing was under 12 viscous units throughout the transition region, which is sufficiently fine according to Jacobs & Durbin (2001).

To verify the grid-resolution requirements in the vicinity of the cylinder, we first examined the two extreme cases, $Re_D = 385$ and 3900. For the low-Reynolds-number case, $Re_D = 385$, near-cylinder resolution was the same as that used by Balaras (2004), who validated the immersed boundary method for the flow past a circular cylinder at $Re_D = 300$ against reference simulations based on boundary conforming grids.

For the high-Reynolds-number case, we performed DNS and LES of the flow past a circular cylinder at $Re_D = 3900$ and compared our results with the DNS data of Kravchenko & Moin (2000). For the LES, we used a computational box of dimensions $L_x \times L_y \times L_z = 30 \times 30 \times \pi$ (with the same spanwise dimension of the domain used by Kravchenko & Moin 2000), which was discretized on a $496 \times 352 \times 80$ grid. The cylinder was located at $x = 10$, $y = 15$. A DNS simulation on the same domain, but using a $608 \times 352 \times 80$ grid (with slightly higher concentration of wall-normal points near the cylinder), produced nearly the same results as the LES. In both cases, the average spacing between adjacent points near the cylinder was 0.015 and 0.011 in the LES and DNS cases, respectively. Free-slip conditions were applied on the top and bottom boundaries, the inlet condition was a uniform streamwise velocity profile, and at the outflow, a non-reflecting convective outflow condition was used (Orlanski 1976). While the simulations of Kravchenko & Moin (2000) are performed using boundary conforming cylindrical grids and a numerical method based on B-splines, our code is based on a rectangular Cartesian grid and uses the immersed boundary method to represent the cylinder; for this reason, we cannot match their grid resolution directly. To ensure a comparable resolution, however, we required the number of immersed boundary points (the points just outside the cylinder surface at which forces are applied to mimic the presence of the body) to be no less than the number of points lying on the cylinder surface in the azimuthal direction in their final grid. In our validation case, we used 210 immersed boundary points along the cylinder countour compared with 185 surface points used by Kravchenko & Moin (2000). At this resolution we obtained very good agreement with their results. Figure 3 presents a comparison of our data with the DNS of Kravchenko & Moin (2000) as well as experiments of Ong & Wallace (1996). Increasing further the number of immersed boundary points to 255 produced no change in the simulation statistics (not shown). With the $Re_D = 385$ and 3900 cases validated and the near-cylinder resolution known for the two cases, we estimated the near-cylinder resolution necessary to ensure accuracy in the $Re_D = 1155$ case. This was done by assuming that the thickness of the laminar boundary layer attached to the cylinder decreases with $\sqrt{Re_D}$, which implies that the $Re_D = 1155$ simulation requires approximately half the near-cylinder resolution of the $Re_D = 3900$ case. For further confidence in the $Re_D = 1155$ results, we also performed the first box of the $Re_D = 1155$ simulation of wake/boundary-layer interaction on a coarser grid, which used only $816 \times 288 \times 96$ to discretize the first box and had 30 % fewer points in each direction near the cylinder. The results of the two simulations were in good agreement, indicating that the fine grid is more than sufficient to resolve the important eddies in the transition region and in the wake.

For the actual $Re_D = 3900$ wake/boundary-layer simulation, we used the same near-cylinder resolution as described above for the validation case. The validity of the laminar boundary-layer solution upstream of the transition region was confirmed by observing agreement with the Blasius solution sufficiently far from the leading edge (where the integral quantities such as displacement and momentum thickness and

https://doi.org/10.1017/S0022112005007342 Published online by Cambridge University Press

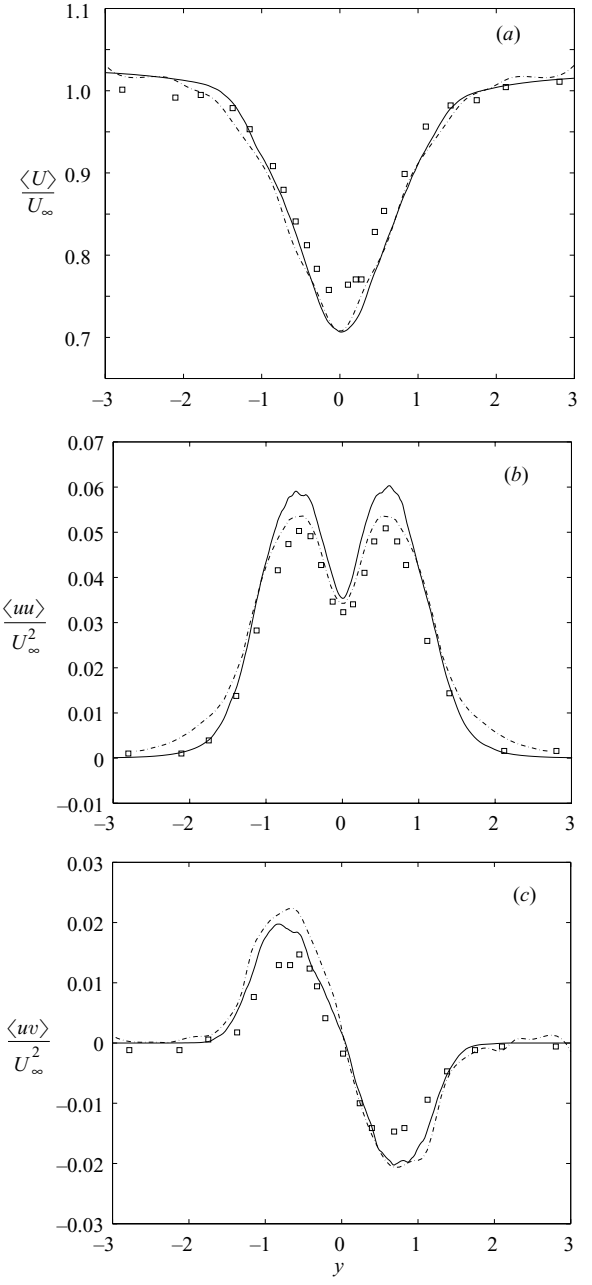


FIGURE 3. Profiles of (*a*) streamwise velocity, (*b*) streamwise Reynolds stress $\langle u'u' \rangle$, (*c*) Reynolds shear stress $\langle u'v' \rangle$ across the cylinder wake at $x = 4$; ———, present LES; □, Experiment (Ong & Wallace 1996); –·–, DNS (Kravchenko & Moin 2000); $Re_D = 3900$.

shape factor matched the analytical solution to within 1 %). At the streamwise location of transition onset ($x = 20$), the boundary layer was resolved with 50 wall-normal grid cells. Throughout the transitional and turbulent regions, the first wall-normal point

https://doi.org/10.1017/S0022112005007342 Published online by Cambridge University Press

was always below $y^+ = 1$. For the $Re_D = 1155$, we ensured that the near-wall region was similarly resolved.

Finally, we examined spanwise two-point correlations of velocity fluctuations to verify that the spanwise size of the computational domain was sufficient for the fuctuations to become decorrelated. Starting from the onset of transition, the correlation in the two velocity fluctuation components decays rapidly to zero, except near the wake centreline, where some spanwise coherence due to the von Kármán street is present throughout the doimain. Upstream of the transitional region, the correlation plots remained oscillatory across the boundary layer, which was due to pronounced streamwise streaky structures existing prior to transition. Some of these observations are illustrated in figure 10, which is discussed in the section on the transition mechanism.

4. Results

4.1. *Flow development*

This section presents an overview of our results for the three Reynolds-number cases considered. Most of the emphasis is placed on the evolution of various flow metrics from the laminar into the turbulent regimes. An examination of the receptivity mechanism and instability is deferred until the next section.

As stated previously, the simulations at $Re_D = 385$ and 3900 were treated by DNS, while in the intermediate-Reynolds-number simulation, the SGS model was included. However, the eddy viscosity was significant only in the near wake of the cylinder (where small scales are generated by the shear-layer instability) reaching maximum values of approximately 1.2 times the molecular viscosity. The grid resolution in the boundary layer was fine enough that the eddy viscosity in that region was negligible, and the transition calculation was effectively a DNS.

In the following, we define time-averaged quantities as

$$F = \langle f \rangle = \frac{1}{L_z}\frac{1}{T}\int_o^{L_z}\int_{t-T}^{t} f(x, y, z, \tau)\,\mathrm{d}\tau\,\mathrm{d}z. \tag{4.1}$$

The integration period, T, was equal to approximately 25 shedding periods and was sufficient to ensure statistical convergence of the data presented herein, as mentioned above.

In our discussion, we will emphasize several statistical flow quantities that change across the laminar–turbulent transition. The skin friction coefficient

$$C_f = \frac{\tau_w}{\rho U_\infty^2/2} \tag{4.2}$$

(where τ_w is the time-averaged wall stress), is an indicator of transition onset since it increases markedly across the laminar–turbulent shift. The shape factor, $H = \theta/\delta^*$, where δ^* and θ are, respectively, the displacement and momentum thicknesses, defined as

$$\delta^* = \int_0^{y_{edge}} \left(1 - \frac{\langle U \rangle}{U_{edge}}\right) \mathrm{d}y; \qquad \theta = \int_0^{y_{edge}} \frac{\langle U \rangle}{U_{edge}} \left(1 - \frac{\langle U \rangle}{U_{edge}}\right) \mathrm{d}y, \tag{4.3}$$

is equal to 2.6 in Blasius flow and is around 1.4 for turbulent flow. It is an inverse measure of the boundary-layer momentum, which increases in the turbulent regime. The integration in (4.3) is performed up to the edge of the boundary layer, y_{edge} (defined as the location of maximum mean velocity between the wake and the plate), and the 'effective' free-stream velocity, U_{edge}, is the mean velocity at this location.

https://doi.org/10.1017/S0022112005007342 Published online by Cambridge University Press

We also examine the near-wall behaviour of the velocity and turbulent kinetic energy (TKE) profiles throughout the domain. In fully turbulent boundary layers, the velocity profile has a logarithmic region, and the TKE profile has a near-wall peak caused by low- and high-speed streaks of streamwise velocity. The log-law expression used in our comparisons is $u^+ = 2.44 \times \log(y^+) + 5.5$. Finally, we will discuss the budget of the TKE across the transitional region $k = \langle u_i' u_i' \rangle / 2$. It is given by:

$$\frac{\partial k}{\partial t} = -\langle U_i \rangle \frac{\partial k}{\partial x_j} - \frac{\partial \langle U_i \rangle}{\partial x_j} \langle u_i' u_j' \rangle - \nu \left\langle \frac{\partial u_i'}{\partial x_j} \frac{\partial u_i'}{\partial x_j} \right\rangle - \frac{1}{\rho} \frac{\partial \langle p' u_i' \rangle}{\partial x_i} + \nu \nabla^2 k - \frac{1}{2} \frac{\partial \langle u_j' u_i' u_i' \rangle}{\partial x_j}. \quad (4.4)$$

The terms on the right-hand side of (4.4), which is derived from the Reynolds-averaged Navier–Stokes (RANS) equations, are referred to, respectively, as advection, production, dissipation, pressure work, viscous diffusion and turbulent transport. Additional SGS production, transport and dissipation terms appear in the $Re_D = 1155$ case, and are included in the RANS production, transport and dissipation, respectively. The sum of the computed terms in the budgets was very small throughout the computational domain, indicating good convergence. For example, in the fully turbulent region, the maximum imbalance was 2 % and 4 % of the maximum production for the $Re_D = 1155$ and $Re_D = 3900$ cases, respectively.

Figure 4 shows instantaneous snapshots of the flow field for each Re_D case. Although the computational domains have different streamwise sizes, the axes limits for the three plots are the same in order to facilitate comparison. Pressure isosurfaces highlight the cylinder wake, and contours of the streamwise velocity fluctuation show the perturbations near the wall as well as in the wake. A more coherent von Kármán vortex street can be observed for the $Re_D = 385$ case than for the $Re_D = 1155$ and 3900 cases. In the higher Re_D cases, consistent with the Reynolds number increase, the cylinder wake contains eddies of a much finer scale. The spanwise rollers of the vortex street rapidly become three-dimensional. Concomitant with the deformations of the rollers, elongated streamwise streaks of high- and low-speed fluid appear inside the laminar boundary layer. In the $Re_D = 385$ case, although the laminar boundary layer is buffeted by the shed vortices, it remains stable and no transition to turbulence is observed within the computational domain. In contrast, in the $Re_D = 1155$ and $Re_D = 3900$ cases, the onset of laminar–turbulent transition is clearly visible at approximately $x = 30$ ($Re_x = 34\,650$) and $x = 20$ ($Re_x = 78\,000$), respectively. Transition is accompanied by significant changes in the mean flow statistics, as well as the generation of fine-scale streaky structures inside the boundary layer. The average spacing between the near-wall streaks is about 100 wall units, consistent with typical turbulent wall-bounded flows. The streaks become visible downstream of $x \simeq 30$ in figure 4(*c*), which extends into the fully turbulent region, but are less clear in figure 4(*b*), which extends only through the middle of the transitional region.

In figure 5, we show the streamwise evolution of skin friction for the three cases. In each case, the skin friction starts from a perturbed laminar value that does not coincide with the Blasius profile. This is due to the combination of the proximity to the leading edge (where Blasius similarity is invalid) and the free-stream acceleration due to the flow obstruction by the cylinder, which causes the initial skin-friction undershoot. In the absence of the cylinder, the Blasius profile was matched by $x = 6$, for the $Re_D = 385$ case. Figures 6 and 7 show profiles of the streamwise velocity at various locations for the three Re_D cases. In figure 7, we have also included profiles of the turbulent kinetic energy at the respective stations.

https://doi.org/10.1017/S0022112005007342 Published online by Cambridge University Press

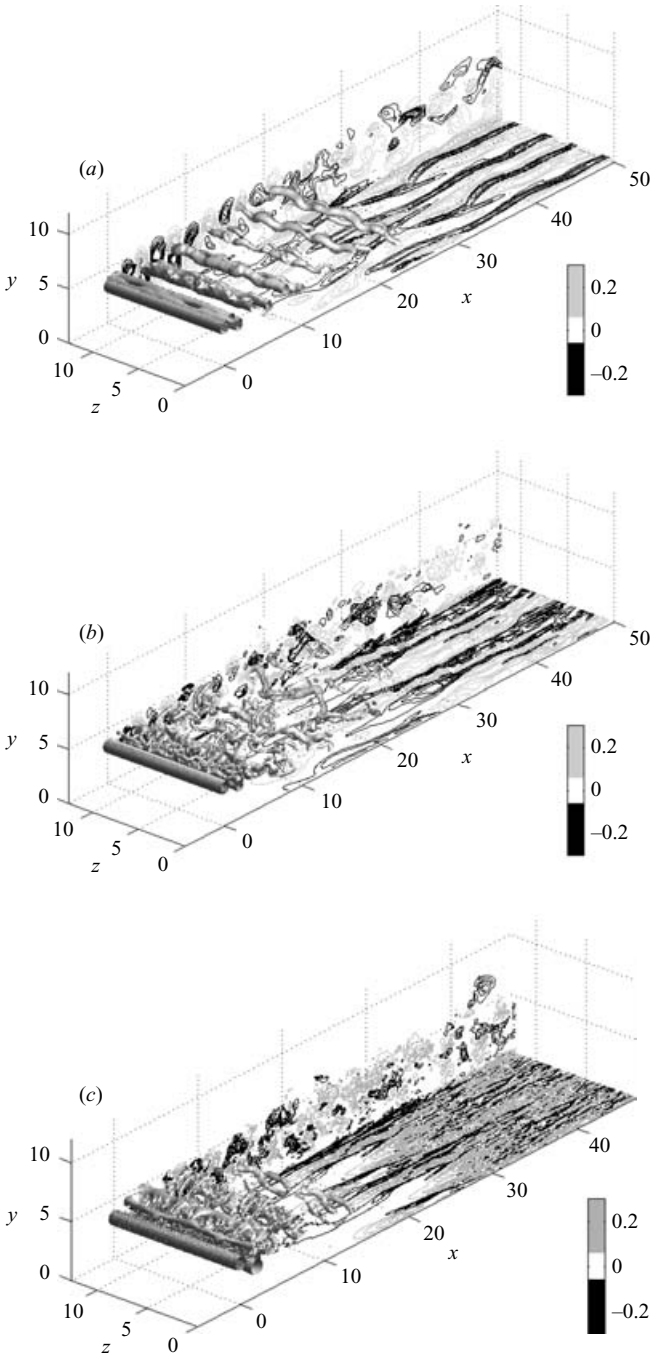


FIGURE 4. Isosurfaces of pressure ($p = -0.08$) and streamwise velocity fluctuation contours inside the boundary layer and in the wake; (*a*) $Re_D = 385$, (*b*) $Re_D = 1155$, (*c*) $Re_D = 3900$.

We begin with a discussion of the statistics for the $Re_D = 385$ case. The skin-friction coefficient shows increasing deviation from the perturbed laminar level, but does not rise more than halfway towards the turbulent value. This behaviour is consistent with evolution of the mean velocity: the velocity profiles show a small progressive

https://doi.org/10.1017/S0022112005007342 Published online by Cambridge University Press

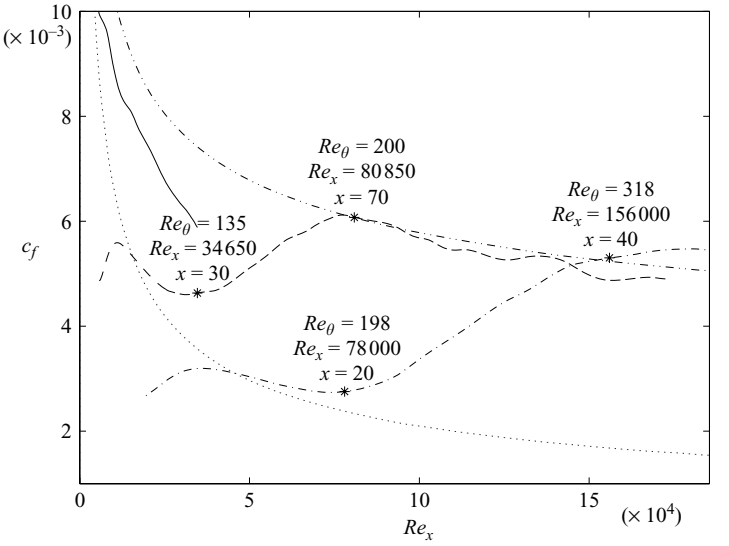


FIGURE 5. Skin friction coefficient; ———, $Re_D = 385$; – – –, $Re_D = 1155$; — · —, $Re_D = 3900$; · · ·, laminar C_f; — · · —, turbulent C_f; the asterisks indicate the locations of the onset and the end of transition.

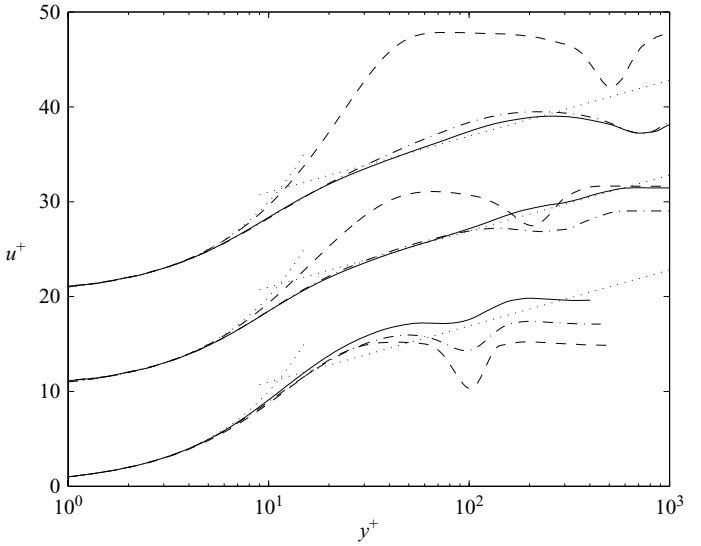


FIGURE 6. Mean streamwise velocity profiles in wall units. Bottom: $Re_D = 385$; – – –, $x = 20$, $Re_x = 7700$; – · –, $x = 50$, $Re_x = 19250$; ———, $x = 90$, $Re_x = 34650$. Middle: $Re_D = 1155$; – – –, $x = 30$, $Re_x = 34650$; – · –, $x = 70$, $Re_x = 80850$; ———, $x = 150$, $Re_x = 173250$. Top: $Re_D = 3900$; – – –, $x = 20$, $Re_x = 78000$; – · –, $x = 40$, $Re_x = 156000$; ———, $x = 47$, $Re_x = 183300$.

deviation from the laminar Blasius solution (figure 7*a*), but there is no trend towards a logarithmic law (figure 6, bottom), and the fuller velocity profile is due to a perturbed laminar flow regime. The shape factor for this case has a minimum value of 2.25, which is below the Blasius value of 2.6, but far from the turbulent value of 1.4. Figure 7 also shows an initial increase in the boundary-layer TKE peak with streamwise

https://doi.org/10.1017/S0022112005007342 Published online by Cambridge University Press

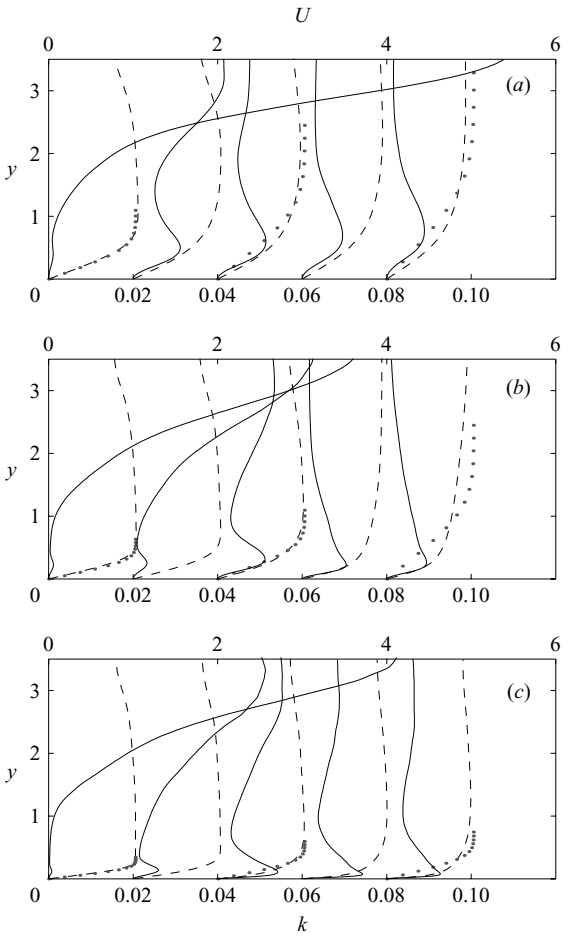


FIGURE 7. Profiles of mean velocity (– – –) and the turbulent kinetic energy (———); (*a*) $Re_D = 385$; from left to right, the plots correspond to $x = 10$, 30, 50, 70, 90, $Re_x = 3850$, 11 550, 19 250, 26 950, 34 650; (*b*) $Re_D = 1155$; from left to right, the plots correspond to $x = 10$, 15, 30, 90, 150, $Re_x = 11\,550$, 17 325, 34 650, 103 950, 173 250; (*c*) $Re_D = 3900$; from left to right, the plots correspond to $x = 10$, 20, 30, 40, 47, $Re_x = 39\,000$, 78 000, 117 000, 156 000, 183 300. The dots correspond to Blasius profiles at the respective Re_x values.

distance, which is most probably due to the growth of the laminar boundary-layer streaks visible in figure 4, which will be discussed in the next section. The TKE peak remains near the middle of the boundary layer and not near the wall as in a turbulent wall-bounded flow. Finally, the Reynolds number based on the momentum thickness, Re_θ, only reaches 105 by the end of the domain ($x = 90$, $Re_x = 34\,650$). To our knowledge, the lowest value of Re_θ at which a turbulent boundary layer can be generated experimentally is 285 (Bandyopadhyay 1987). In our $Re_D = 1155$ calculation, the boundary layer had fully turbulent statistics at $Re_\theta \simeq 200$.

For the $Re_D = 1155$ case, the C_f curve begins to rise at $x = 30$ ($Re_x \simeq 35\,000$), indicating the onset of transition. The skin-friction maximum (which may be viewed as the end of transition) is attained at $x \simeq 70$ ($Re_x \simeq 81\,000$). We note in passing that this Reynolds number is far below the range characteristic of transition due to Tollmien–Schlichting (TS) waves $\left(Re_x \simeq 10^6\right)$. The low transitional Re_x value is more

https://doi.org/10.1017/S0022112005007342 Published online by Cambridge University Press

consistent with bypass transition due to moderate-amplitude free-stream turbulence (e.g. Roach & Brierlay 1992).

The skin-friction development at $Re_D = 3900$ indicates that transition to turbulence begins at $x \simeq 20$ ($Re_x = 78\,000$) and is complete by $x = 40$, or $Re_x = 156\,000$. Also visible is a pronounced skin friction overshoot of the values predicted by the calculation in the turbulent region. As mentioned earlier, we met or exceeded the standard grid resolution requirements for a turbulent boundary layer, so the overshoot is probably not due to a lack of resolution. Unfortunately, our computational domain did not extend beyond location $x = 47$, so the behaviour of the skin-friction farther downstream remains unknown for this case.

The velocity profiles for the $Re_D = 1155$ and 3900 cases (figure 7*b*, *c*) indicate a greater deviation from the Blasius profile than observed for $Re_D = 385$, starting at locations $x \simeq 50$ and $x \simeq 30$ ($Re_x = 57\,750$ and $Re_x = 117\,000$), respectively. Figure 6 (middle and bottom) shows that the mean near-wall streamwise velocity profiles at $Re_D = 1155$ and $Re_D = 3900$ develop a logarithmic layer, suggesting that a turbulent equilibrium is established. For the $Re_D = 3900$ case, we observe a momentum deficit in the wake, even where the velocity profile appears turbulent. This is because the development of statistical quantities in the wake is x-dependent and not Re_x-dependent, as will be discussed later. For both Re_D cases, the shape factor reaches a value of approximately $\simeq 1.5$ consistent with low-Reynolds-number turbulent flow. The TKE profiles in figures 7(*b*) and 7(*c*) show that by the locations $x = 50$ ($Re_D = 1155$) and $x = 30$ ($Re_D = 3900$), the boundary-layer peak is moving closer to the wall. At $x = 100$ ($Re_x = 115\,500$) and $x = 41$ ($Re_x = 160\,000$) for the lower and higher Re_D cases, respectively, the position of the peak was about 15 wall units, close to the accepted value of 12 for near-wall turbulent flows. The evolution of boundary-layer TKE will be discussed at greater length in the next section in the context of the mechanism of transition.

The budgets of the TKE were also computed for each case. Figure 8 shows the development of the TKE budget corresponding to the $Re_D = 1155$ simulation. We focus on this case, but the differences from the other cases will be noted. The data are normalized by the free-stream velocity and cylinder diameter. This choice was made in order to separate the effects of the mean flow evolution (which enters through the change in u_τ) from the evolution of the budget terms, which involve higher-order moments. The figure illustrates that the boundary-layer TKE production maximum is initially near the middle of the laminar boundary layer. The location of the peak approximately coincides with the location of the maximum u_{rms}. As the perturbed laminar boundary grows, the peak in the production slowly moves farther away from the wall, up to the onset of transition at $x = 30$; beyond this location, it moves rapidly toward the wall. While the wake is strong, ($x < 30$), turbulent transport (the dashed line in figure 8) increases the boundary-layer turbulence by convecting wake turbulence into the outer part of the boundary layer. In this region, the dissipation and the turbulent transport inside the boundary layer are small and the budgets are balanced by the advection term (unlike fully turbulent boundary layers, in a transitional boundary layer, owing to a rapid growth of the TKE, the term $-\langle U\rangle \partial k/\partial x$ is significant). By $x = 30$ ($Re_x = 34\,650$), (figure 8*b*) the magnitudes of the budget terms are about 2/3 of their turbulent values; and by $x = 47$ ($Re_x = 54\,285$), the budget is nearly that of a turbulent near-wall flow. At this location the near-wall streamwise velocity profile does not yet have a logarithmic region; the laminar–turbulent shift in the mean velocity profile occurs after a near-wall turbulence cycle has been established. At the final location, $x = 90$ ($Re_x = 183\,300$), we are also showing the turbulent channel data of Moser, Kim & Mansour (1999) obtained at $Re_\tau = 395$

https://doi.org/10.1017/S0022112005007342 Published online by Cambridge University Press

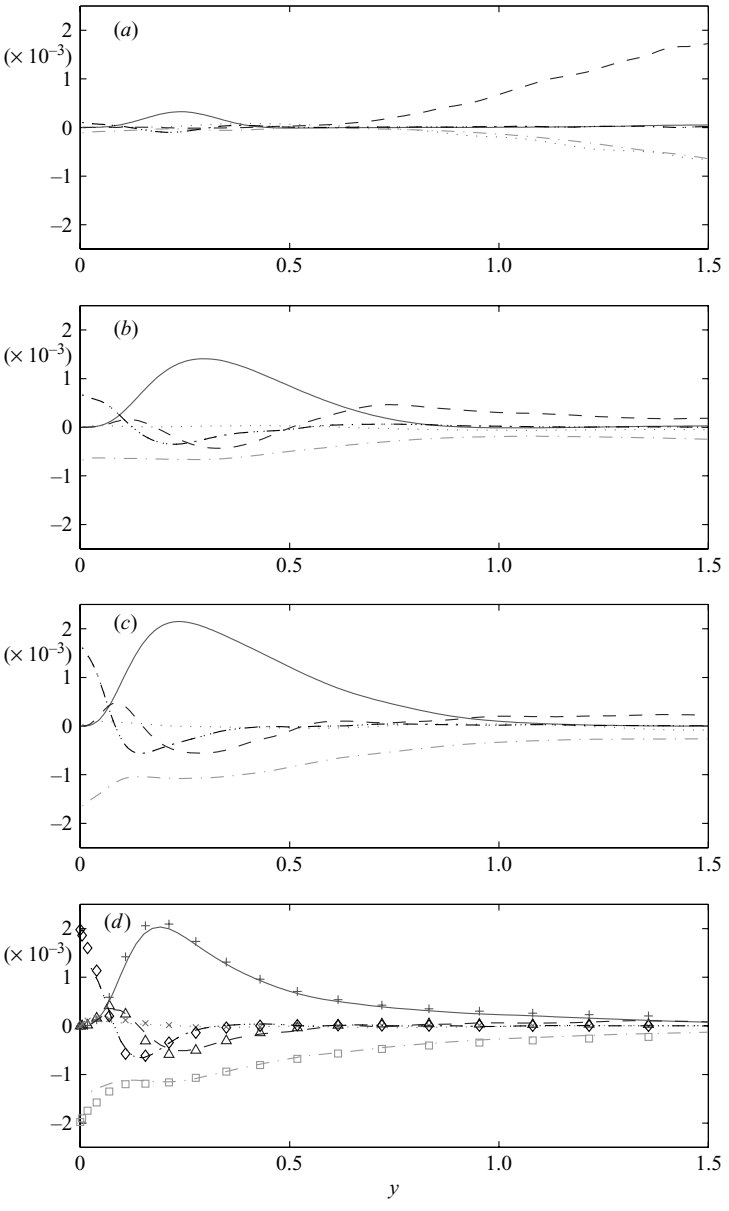


FIGURE 8. Budgets of k at various locations; $Re_D = 1155$. All terms are normalized by U_∞ and D. (*a*) $x = 15$, $Re_x = 17\,325$, $\delta_{99} = 0.51$; (*b*) $x = 30$, $Re_x = 34\,650$, $\delta_{99} = 0.92$; (*c*) $x = 47$, $Re_x = 54\,285$, $\delta_{99} = 1.18$; (*d*) $x = 90$, $Re_x = 103\,950$, $\delta_{99} = 2.1$. Symbols: channel flow DNS by Moser *et al.* (1999); lines: present simulation. +, ———, production; □, — · —, dissipation; △, – – –, turbulent transport; ×, · · ·, pressure diffusion; ◇, — · · —, viscous diffusion.

for comparison (the use of channel rather than boundary-layer data for comparison is justified because the near-wall behaviour of the two flows is very similar). To convert the channel data to outer coordinates, we used the local u_τ and ν from our simulation. The comparison in figure 8(*d*) shows that a turbulent equilibrium is fully established. An examination of the TKE budgets for the $Re_D = 3900$ case revealed a similar development, except that between locations $x = 26$ and $x = 40$, the

https://doi.org/10.1017/S0022112005007342 Published online by Cambridge University Press

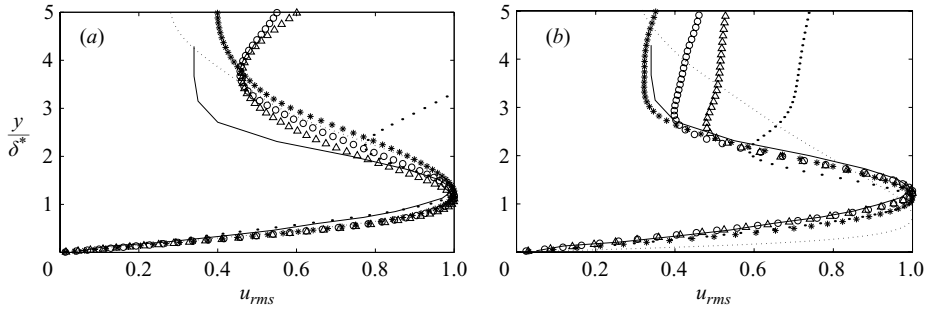


FIGURE 9. Profiles of u_{rms} across the boundary layer normalized by the maximum boundary-layer u_{rms}; δ^* is the displacement thickness; (*a*) $Re_D = 385$; ●, $x = 10$; △, $x = 30$; ○, $x = 40$; ⋆, $x = 60$; ···, $x = 90$; (*b*) $Re_D = 3900$; ●, $x = 5$; △, $x = 10$; ○, $x = 15$; ⋆, $x = 20$; ···, $x = 30$; ———, from Matsubara & Alfredsson (2001).

dissipation at the wall exceeds the peak energy production inside the boundary layer. The near-wall peak in the turbulent transport is about 50 % of the peak production, compared to 25 % which is typical of near-wall turbulent flows. By location $x = 47$ ($Re_x = 183\,300$), the TKE budget is again very close to the data of Moser *et al.* (1999), indicating that a turbulent equilibrium has been reached. The development of the TKE budget corresponding to the $Re_D = 385$ case was similar to that of the $Re_D = 1155$ case prior to the transition onset. The y-location of the turbulence production peak increases throughout the computational domain, and the magnitude of the peak increases initially, then decreases downstream of $x = 20$, ($Re_x = 6700$), indicating that the perturbation is decaying.

4.2. *Instability and laminar breakdown*

The purpose of this section is to identify the important stages in flow evolution prior to the onset of fully developed turbulence. We focus our attention primarily on the $Re_D = 385$ and $Re_D = 3900$ cases; the intermediate $Re_D = 1155$ case combines elements from both. Much of our discussion will be inspired by the $Re_D = 385$ case data, since the low Reynolds number implies a narrower range of scales which makes the identification of coherent structures easier. Many of the observations regarding this case carry over to the higher Re_D cases, although important differences will be pointed out in the course of the discussion.

Visualizations of the three flow fields in figure 4 were discussed in the previous section. The prominent difference between the cases is in range of flow scales, which increases with Reynolds number. The higher the Reynolds number, the more rapidly the wake loses its coherence, and the more unstable the boundary layer is to perturbation. Despite the difference in the Reynolds number, we believe that the mechanism of interaction is the same in all three cases, as described below.

The visualizations in figure 4 show the generation of streamwise velocity streaks downstream of location $x \simeq 10$ for all cases. To characterize these streaks, we computed profiles of u_{rms} inside the perturbed boundary layer, shown in figure 9 for the $Re_D = 385$ and $Re_D = 3900$ cases. When the wall-normal coordinate is scaled with the local displacement thickness, and u_{rms} with its maximum inside the boundary layer, the profiles exhibit a region of approximate self-similarity. For the $Re_D = 385$ case, the self-similar region is established at $x \simeq 20$ and persists downstream, as the boundary layer remains laminar. For the $Re_D = 3900$ case, this region is limited to the range $x \in [10, 20]$. Farther downstream, transition to turbulence occurs, and the location

https://doi.org/10.1017/S0022112005007342 Published online by Cambridge University Press

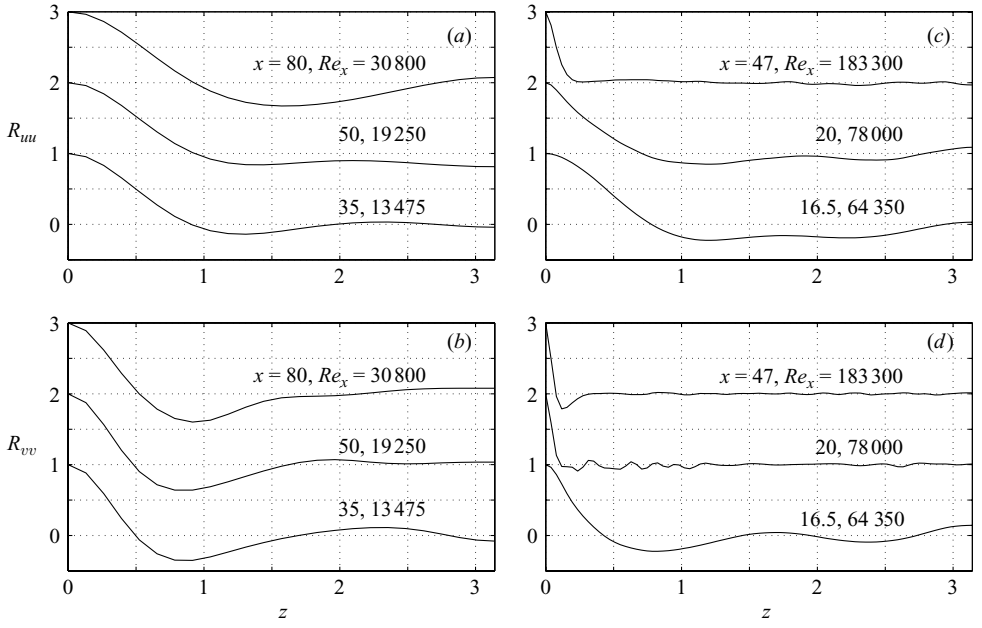


FIGURE 10. Spanwise correlation functions of the streamwise and wall-normal velocity fluctuations; (*a*) $Re_D = 385$, R_{uu}; (*b*) $Re_D = 385$, R_{vv}; (*c*) $Re_D = 3900$, R_{uu}; (*d*) $Re_D = 3900$, R_{vv}; the correlation functions are computed at $y = 0.2$.

of the u_{rms} peak shifts towards the wall. In the figure we also show experimental data of Matsubara & Alfredsson (2001), which was obtained from a transitional boundary layer subjected to moderate free-stream turbulence. The agreement with measured data is good, indicating that the streaks found in our simulations may be related to the Klebanoff modes (Klebanoff 1971) observed in the experiment. We note that the self-similarity is approximate: the peak in u_{rms} moves closer to the wall with increasing Reynolds number. This trend is also present in the experiments of Mastubara & Alfredsson (2001) and in the numerical simulations of boundary-layer transition due to f.s.t. by Brandt *et al.* (2004).

To determine the average spacing between the streaks, we computed spanwise correlation functions of streamwise and wall-normal velocity fluctuations. In figure 10, we plot these functions for the $Re_D = 385$ and $Re_D = 3900$ cases at various streamwise positions at $y = 0.2$. The first streamwise location for each Reynolds number was chosen to match the approximate onset of streak self-similarity. Both R_{uu} and R_{vv} correlations in figures 10(*a*) and 10(*b*) predict an average streak spacing of $2.5D$ at $Re_D = 385$ (twice the distance to the first R_{uu} minimum, or four times the distance to the first R_{vv} minimum). For this case, the streak spacing remains approximately constant throughout the domain. The bottom curves in figures 10(*c*) and 10(*d*) corresponding to $Re_D = 3900$, are also consistent with streamwise streaks separated by $\simeq 2.5D$. For the intermediate case, $Re_D = 1155$, the streak spacing was estimated to be the same. This finding may seem surprising, since there is a factor of five difference in Re_x between the highest and the lowest Reynolds number. The boundary-layer thickness δ_{99} is 1.59 for the $Re_D = 385$ case at location $x = 35$ and 0.35 for the $Re_D = 3900$ case at location $x = 16.5$. Thus, there is also a factor of 4.5 difference in δ_{99}. At the above locations, the streaks are $1.6\delta_{99}$ and $7.2\delta_{99}$ apart for the two

https://doi.org/10.1017/S0022112005007342 Published online by Cambridge University Press

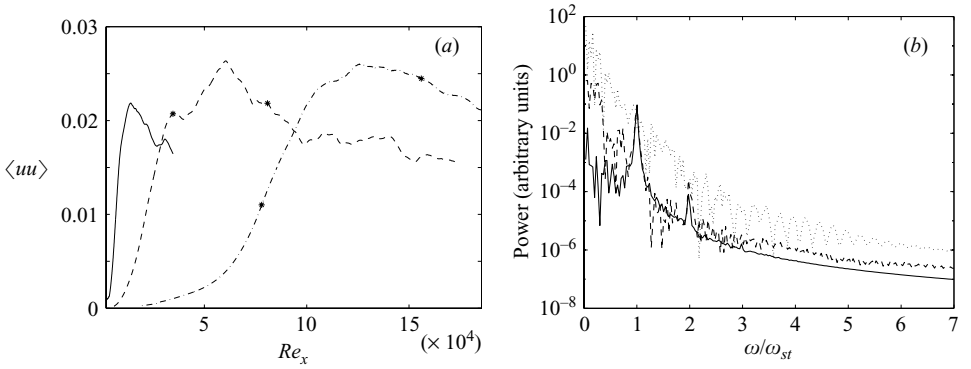


FIGURE 11. (*a*) Maximum streamwise Reynolds stress $\langle uu \rangle$ inside the boundary layer. ———, $Re_D = 385$; – – –, Re_1, 155; — · —, $Re_D = 3900$; (*b*) Spectra of streamwise velocity inside the boundary layer for the $Re_D = 385$ case; ———, $x = 0$; – – –, $x = 10$; · · ·, $x = 30$.

cases, respectively. Experiments and simulations on boundary-layer transition due to moderate to strong levels of f.s.t (e.g. Jacobs & Durbin 2001; Matsubara & Alfredsson 2001), in contrast, report streamwise streaks with mean separation of the order of the boundary-layer thickness. An explanation of this discrepancy is given below when we discuss the evolution of the cylinder wake.

Figures 10(*c*) and 10(*d*) also show spanwise correlation functions at location $x = 20$, at the onset of transition, and at $x = 47$ when the flow is fully turbulent. An abrupt decrease in streak spacing to $0.5D$ is evident; these streaks are different from those described above and characterize the near-wall region of turbulent wall-bounded flows. At location $x = 20$, the R_{vv} curve already shows small-scale fluctuations, whereas the R_{uu} curve is little different from the one at location 16.5, suggesting that instability leading to turbulence first manifests itself through the wall-normal velocity component (the correlation function for the spanwise velocity fluctuation, R_{ww}, was very similar to R_{uu}).

In figure 11(*a*), we show the maximum streamwise Reynolds stress $\langle uu \rangle$ inside the boundary layer for the three Re_D cases. The stars indicate the locations of the onset of transition and the C_f maximum. All three curves exhibit a region of rapid growth followed by a slow decrease. For the $Re_D = 1155$ and $Re_D = 3900$ cases, we note an overshoot of $\langle uu \rangle$ within the transitional region. A similar overshoot upstream of the onset of turbulence is also documented in the studies of bypass transition due to free-stream turbulence by Matsubara & Alfredsson (2001) and is probably a general feature of boundary-layer bypass transition.

To determine whether the initial growth of the streamwise Reynolds stress in our simulations is localized to a particular band of frequencies, we computed frequency spectra of streamwise velocity fluctuation at various locations in the domain. Figure 11(*b*) shows frequency spectra for the $Re_D = 385$ case at the streamwise locations $x = 0$, $x = 10$ and $x = 30$, corresponding to $Re_x = 0$, $Re_x = 3850$ and $Re_x = 11\,550$. The higher two Re_x values are within the rapid growth region, which extends to $Re_x \simeq 14\,000$. The wall-normal location was $y = 0.1$ for the three curves, which falls inside the bottom 15 % of the boundary layer for the two downstream stations. The frequency axis is normalized with $\omega_{St} = 0.215$, corresponding to the Strouhal frequency of wake shedding. A peak corresponding to the shedding frequency of the cylinder can be seen at the first two locations. This peak is caused by the instant

https://doi.org/10.1017/S0022112005007342 Published online by Cambridge University Press

propagation of the unsteadiness of the cylinder wake shedding through the pressure. The peak becomes less prominent with downstream distance, and by location $x = 40$, it is completely obscured by the presence of the neighbouring frequencies. We also note the initial presence of two higher-order harmonics of the Strouhal frequency. Only one harmonic was detected for the $Re_D = 3900$ case, perhaps because the signal was more noisy at this Reynolds number. The presence of harmonics was also noted by Kyriakides *et al.* (1996) during their experiment.

More significantly, figure 11(*b*) indicates that most of the growth in the $\langle uu \rangle$ Reynolds stress at $Re_D = 385$ occurs within the low-frequency range, at or below 1/4 of the shedding frequency of the cylinder. This observation is consistent with the growth of the streamwise streaks inside the boundary layer with the downstream distance. A growth region similar to ours has been noted in experiments on bypass transition due to f.s.t. (e.g. Klebanoff 1971), which is caused by the growth of low-frequency Klebanoff modes inside the perturbed boundary layer. Several experiments showed that the streamwise Reynolds stress grows in proportion with the flat-plate Reynolds number Re_x, although the constant of proportionality is not agreed upon (see Westin *et al.* 1994 for further discussion). In our simulations, we do not see a well-defined linear growth region. This is most probably because the disturbance does not interact with the boundary layer starting from the leading edge, or that the disturbance environment associated with strong wake/boundary-layer interactions is different from f.s.t. Outside the boundary layer in the wake region, we did not observe energy growth in the low frequencies; the amplitude of the Strouhal frequency remained dominant through the entire computational domain.

The spectra corresponding to the $Re_D = 3900$ case (not shown) had a similar behaviour for the low-frequency modes in the rapid growth region. Downstream of location $x = 20$, we observed rapid growth in high frequencies, characteristic of the breakdown to turbulence. No spectra were obtained for the $Re_D = 1155$ case.

The behaviour of disturbance spectra is in partial agreement with the experiments of Kyriakides *et al.* (1999). Although their configuration was slightly different, with the cylinder axis located one diameter upstream of the plate and the Reynolds number set to 3500, the important features of the flow should be comparable between the two cases. Kyriakides *et al.* (1999) were able to detect velocity fluctuations at the Strouhal frequency inside the boundary layer within the Reynolds number range $Re_x = 24\,500$–$59\,500$. They used the velocity signal to deduce the presence of a secondary vortical structure located within the boundary layer, which was induced by a von Kármán vortex with negative spanwise vorticity. They did not, however, report any structures with large streamwise scales, which are prominent in our simulations. This may be because they did not place probes sufficiently far downstream of the leading edge. In our $Re_D = 3900$ simulation, streamwise streaks were clearly visible at $x \simeq 16$, corresponding to $Re_x = 62\,400$ (see figure 10). We did not observe any spanwise vortical structures inside the boundary layer. However, Kyriakides *et al.* (1996) presented streamwise velocity spectra at $Re_D = 385$, which had a pronounced growth in the low-frequency content, consistent with the presence of long streamwise scales.

To investigate the connection between the cylinder wake and boundary-layer streaks, we examined the instantaneous flow field for the three Re_D cases. In figure 12, isosurfaces of pressure fluctuation (grey) are superimposed on top of streamwise velocity fluctuation contours inside the boundary layer for the $Re_D = 385$ and $Re_D = 3900$ cases. For the low Re_D case, we also show isosurfaces of positive streamwise vorticity fluctuation (light grey) and isosurfaces of negative streamwise

https://doi.org/10.1017/S0022112005007342 Published online by Cambridge University Press

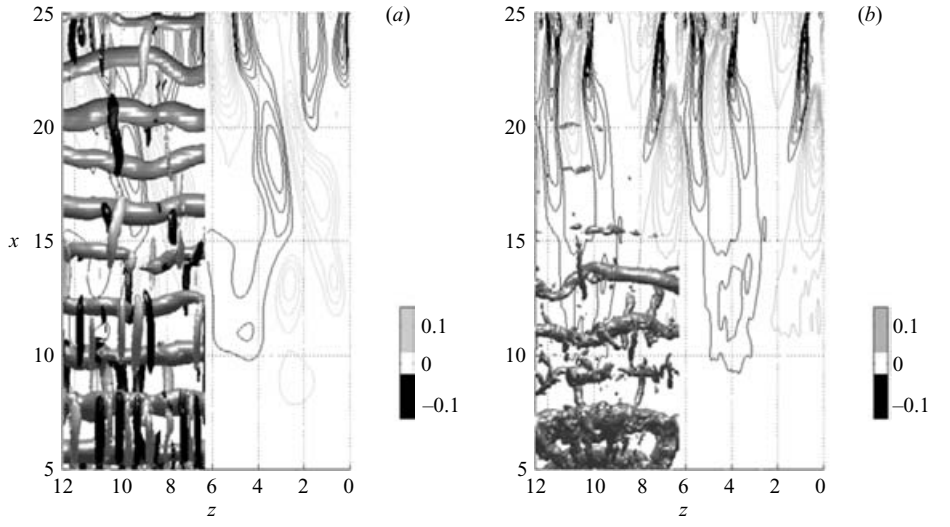


FIGURE 12. Isosurfaces of pressure (grey, $p = -0.08$), isosurfaces of positive (light grey, $\omega_x = 1$) and negative (black, $\omega_x = -1$) streamwise vorticity fluctuation above contours of streamwise velocity fluctuation inside the boundary layer; vorticity is shown only for the $Re_D = 385$ case. (*a*) $Re_D = 385$, contours are plotted at $y = 0.4$ (*b*) $Re_D = 3900$, contours are plotted at $y = 0.1$.

vorticity fluctuation (black). The pressure isosurfaces highlight large spanwise vortices behind the cylinder and the vorticity isosurfaces show the braid vortices around the spanwise rollers. Vorticity isosurfaces are omitted for the $Re_D = 3900$ case because they do not correspond to coherent structures at this higher Reynolds number, i.e. the braid vortices break down to fine-scale turbulence early on. The domain is repeated in the spanwise direction in order to show the boundary-layer streaks more clearly.

The pressure isosurfaces become wavy with downstream distance, indicating the deformation of the spanwise rollers. The dominant spanwise wavelength of this deformation is equal to about half of the domain size for both cases, around $3D$. This value is in agreement with experimental data for the mode A instability of the cylinder wake at low Reynolds numbers (see Williamson 1996). For the high Re_D case, no data are available for comparison. That this wavelength seems the same for two simulations separated by a factor of 10 in the Reynolds number implies a weak Reynolds-number dependence.

From the contours of u' inside the boundary layer and the spanwise correlation data presented earlier, it appears that the streaks occur on the same spanwise scale as the deformation of the rollers. They are unlikely to be induced by the braid vortices (which correspond to the mode B instability of the cylinder wake), whose spanwise length scale is smaller, approximately $1D$, for the $Re_D = 385$ case, and which have nearly degenerated into small-scale turbulence by location $x = 10$ for the $Re_D = 3900$ case. In both cases (and also for $Re_D = 1155$, not shown), well-defined streaks appear at location $x \approx 15$. The fact that this location is the same at $Re_D = 385$ and $Re_D = 3900$, despite a factor of three difference in the boundary-layer δ_{99} between the two cases, indicates that for this flow configuration, the location of streak inception is not very sensitive to the Reynolds number. To gain more insight into the mechanism of streak generation, we examined a time sequence of velocity fluctuations in a cross-stream plane located at $x = 10$ for the $Re_D = 385$ case. When the plane cut across a spanwise roller, the contours of the streamwise velocity fluctuation were sinusoidal in the core

https://doi.org/10.1017/S0022112005007342 Published online by Cambridge University Press

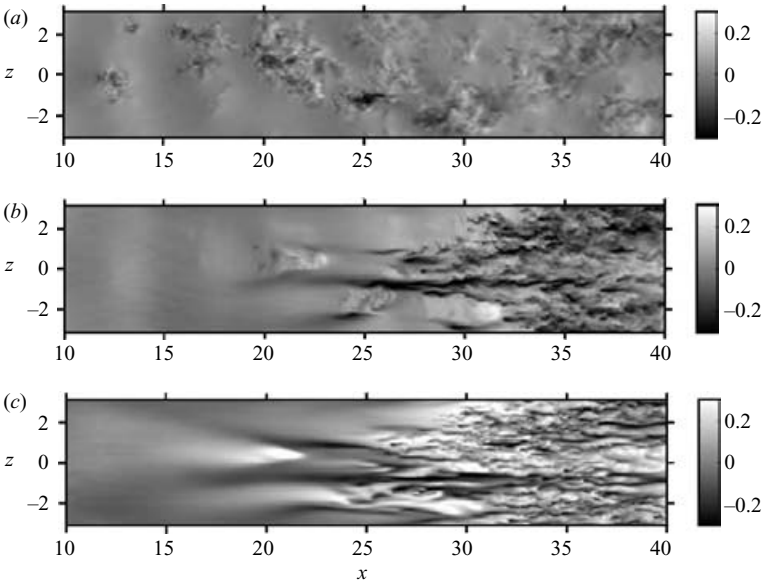


FIGURE 13. Contours of instantaneous streamwise velocity fluctuation; (*a*) $y = 0.1$, (*b*) $y = 0.3$, (*c*) $y = 1.0$. At $x = 10$: $Re_x = 39\,000$, $\delta_{99} = 0.28$; at $x = 40$: $Re_x = 156\,000$, $\delta_{99} = 0.79$, $Re_D = 3900$.

of the vortex, consistent with the deformation of the roller in the (x, z)-plane. Such deformation partially reorients the spanwise vorticity of the roller in the streamwise direction. The streamwise-oriented sections of the roller inject fluid into the boundary layer that gives rise to laminar velocity streaks.

While cross-stream planes proved useful for the $Re_D = 385$ case, for the $Re_D = 3900$ case they were more difficult to interpret because of finer-scale structures present in the flow. A different perspective is provided in figure 13, which shows contours of the streamwise velocity fluctuation at three (x, z)-planes, located at $y = 1$, 0.3 and 0.1, top to bottom. The boundary-layer thickness, δ_{99}, is 0.28 at $x = 10$, and 0.79 at $x = 40$. The top plane, located outside the boundary layer, shows patches of small-scale turbulence occurring at intervals of length five, close to the Strouhal wavelength of wake shedding. This is consistent with the wake ejecting fluid towards the boundary layer. The patches located at $x \simeq 20$ and $x \simeq 25$ are also visible in the middle and bottom planes, both of which are within the boundary layer at these locations. The bottom plane also shows two low-speed streaks surrounding the patch of high-speed turbulence ejected from the wake at $x \simeq 20$. Thus, it appears that at $Re_D = 3900$, the laminar velocity streaks are the direct result of turbulence ejected by the wake into the boundary layer. Unfortunately, we do not have time series of the velocity field or (x, z)-planes at $Re_D = 3900$, which could confirm the connection between wake turbulence and the boundary-layer streaks at $Re_D = 3900$. Instead, the above discussion is supported by two instantaneous velocity fields.

Because the cylinder Reynolds number is sufficiently high at 3900, the streaks become unstable and rapidly break down to turbulence. The region of breakdown is intermittent; the intermitency may be visualized from plots of skin friction at different instants in time. Figure 14 shows the temporal evolution of instantaneous (spanwise-averaged to remove high-frequency noise) skin friction. The intermittency is similar to the turbulent spots found in bypass transition studies (see Jacobs & Durbin 2001; Matsubara & Alfredsson 2001). We can see high C_f regions associated with

https://doi.org/10.1017/S0022112005007342 Published online by Cambridge University Press

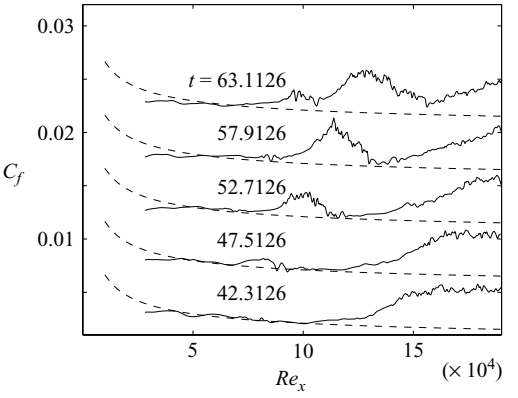


FIGURE 14. Instantaneous spanwise-averaged and time- and spanwise-averaged skin friction coefficient; ———, instantaneous C_f; – – –, Blasius C_f; $Re_D = 3900$.

turbulence moving downstream, as the peak C_f inside the region is also increasing. Note, in particular, the curve corresponding to $t = 57.9$, which shows a turbulent region surrounded by low skin-friction values, indicating the presence of turbulence inside laminar flow. From the instantaneous skin-friction plots, we estimated the convective speeds of the front and the rear of an intermittency region to be $0.99U_\infty$ and $0.66U_\infty$, respectively. These values are higher than those reported by Henningson, Spalart & Kim (1987), who simulated the development of a 'classical' arrowhead-shaped turbulent spot, and found convection velocities of $0.9U_\infty$ and $0.5U_\infty$, respectively. These differences may be due to the different types of boundary-layer disturbance in the two simulations, as was suggested by Jacobs & Durbin (2001); Henningson *et al.* (1987) introduced a disturbance near the wall, whereas in our case, the disturbance entered the boundary layer from the free stream. Finally, it is not clear whether, in the present case, the intermittency is due entirely to streak instability or to the impingement of wake turbulence on the boundary layer. The intermittency was not observed for the $Re_D = 1155$ case, probably because the Reynolds number was not sufficiently high.

In summary, we have found that the interaction of a cylinder wake with a flat-plate boundary layer results in the generation of streamwise streaks that in the high Re_D cases breakdown to turbulence. The profiles of u_{rms} inside the boundary layer indicate that the streaks are similar to Klebanoff modes (Klebanoff 1971). A rapid initial growth in the low-frequency components of the streamwise velocity spectrum suggests that the incipient streaks are preferentially amplified inside the boundary layer. The streaks appear to be generated by the three-dimensional instability of the primary vortex in the wake. The scale of this instability is approximately the same for the three cases, which results in the same spacing between the boundary-layer streaks for the three Reynolds numbers. The proposed mechanism is an example of strong interaction, i.e. one in which the disturbance acting on the boundary layer is coherent. We also found that the transitional region in the $Re_D = 3900$ is intermittent and similar to that in bypass transition due to f.s.t.

As mentioned previously, Kyriakides *et al.* (1996) carried out experiments on wake-induced boundary-layer transition for several Reynolds numbers, including $Re_D = 385$, $Re_D = 1155$ and $Re_D = 3500$. They observed transition in all three cases, respectively, at $x = 7.3$, 2.7 and 54.5, corresponding to $Re_x = 2625$, for the first two cases, and 21 000 for the last. They stated that the transition scenario is the same for all

https://doi.org/10.1017/S0022112005007342 Published online by Cambridge University Press

three cases. Unfortunately, a meaningful comparison of our simulations with their experiments is difficult, primarily because the indicator of boundary-layer transition used in their work is only qualitative. Kyriakides *et al.* (1996) state that 'the x-location where the [streamwise] velocity signal loses its sinusoidal character is considered to be the onset of transition.' The velocity spectra obtained for our $Re_D = 385$ case show that the peak corresponding to the Strouhal frequency inside the boundary layer disappears by location $x = 40$. At this location, the velocity signal is certainly non-sinusoidal. However, as we have shown, the flow does not transition to turbulence inside the domain. The observation that the momentum thickness Reynolds number was 105 at $Re_x = 34\,650$, further suggests that it is improbable, if not impossible, to see transition at $Re_D = 385$ within the flow region considered. Furthermore, the experimental observation that, at $Re_D = 1155$, the onset of transition occurs at a distance from the leading edge smaller than the distance between the cylinder and the plate, cannot be caused by the response of the boundary layer to wake turbulence (which would imply particle trajectories that form an angle greater than 45° to the wake centreline). Instead, it suggests that the phenomena observed in the experiment are due to the advection caused by the von Kármán street and reflect the wake breakdown more than the boundary-layer response to the perturbation. Thus, the loss of a sinusoidal character may not be an appropriate measure of transition. Instead, it may be an indicator of the onset of a perturbed flow regime inside the boundary layer that may lead to transition farther downstream.

4.3. *Onset of turbulence*

The ability to predict and control the onset of transition is the ultimate goal in theoretical and applied transition studies. Although our simulations span only a decade in the Reynolds-number range, we can use the present data to make a conjecture on the effect of increasing the cylinder Reynolds number on transition onset. The location of the cylinder inside the domain is another important variable, and its effects on transition should be investigated in a future study.

Figure 5 shows skin-friction coefficients for the three cases as a function of Re_x. The curves do not collapse under the Re_x scaling; in fact, the onset of transition in the high-Reynolds-number case occurs at an Re_x value that is more than twice as large for $Re_D = 1155$. To understand this behaviour, we compare in figure 15 contours of the spanwise vorticity in an (x, y)-plane in the transition region for the two cases. This figure shows that the wake spreading is very similar for the two cases, i.e. it is a weak function of the Reynolds number. An obvious difference in the range of turbulent scales is present because of the factor of three difference in the Reynolds numbers. The boundary layer is also much thinner in the $Re_D = 3900$ case, since $\delta \sim Re^{1/2}$. Because of the weak Reynolds-number dependence of the wake spreading, the boundary layer and the wake interact at approximately the same distance from the leading edge for the three cases. Direct impingement of the wake turbulence on the boundary layer can be visually observed as close upstream as $x = 15$ at some instances; the visualization in the figure shows wake turbulence impinging on the boundary layer around $x = 20$ for all three Reynolds numbers. The figure also shows that the mean velocity profile loses its inflection points near location $x = 40$ ($x = 39$, 38 and 42, for the three Re_D cases, from lowest to highest), indicating that the location of the merger between the wake and the boundary layer is relatively insensitive to the cylinder Reynolds number. However, once the boundary layer has been perturbed, the Reynolds-number effect becomes important: the higher the Reynolds number, the more rapid the breakdown to turbulence.

https://doi.org/10.1017/S0022112005007342 Published online by Cambridge University Press

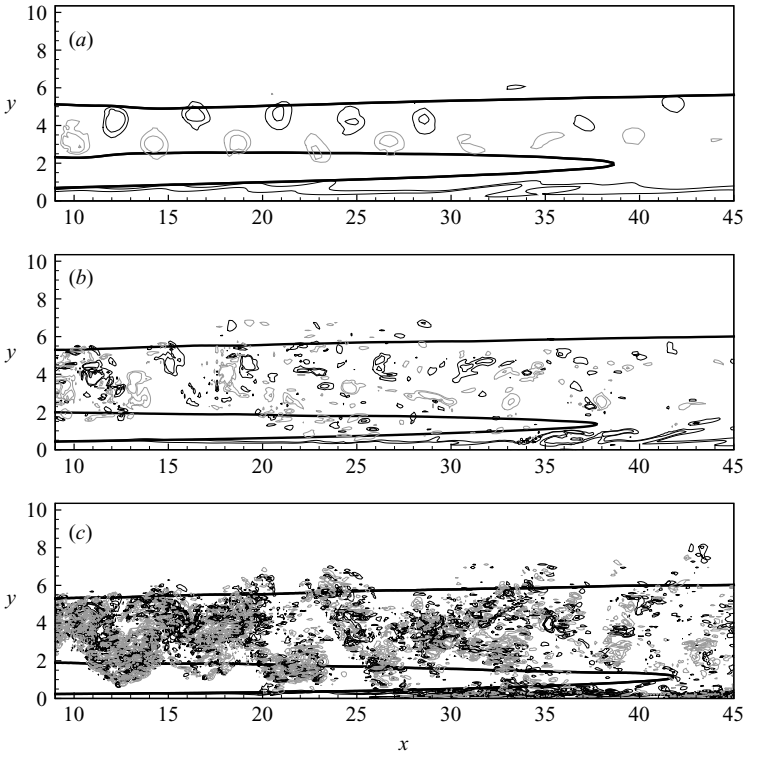


FIGURE 15. Contours of the spanwise vorticity. (*a*) $Re_D = 385$; (*b*) $Re_D = 1155$; (*c*) $Re_D = 3900$. Contour levels are ± 0.5 and ± 1; negative contours are grey. The thick lines are $U = 1$ isolines, showing the wake and boundary-layer thickness.

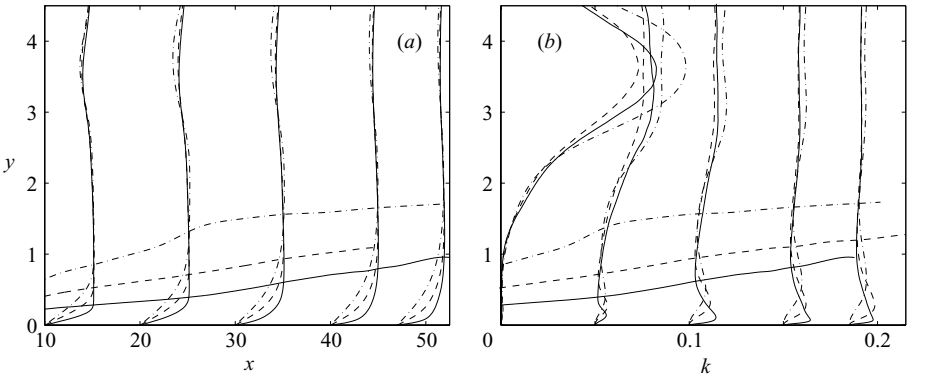


FIGURE 16. Profiles of (*a*) streamwise velocity and (*b*) TKE at locations $x = 10$, 20, 30, 40, 47 from left to right. ———, $Re_D = 3900$; – – –, $Re_D = 1155$; — · —, $Re_D = 385$; the horizontal lines represent the boundary-layer thickness for each case. In (*a*), the velocity profile is amplified by a factor of five for clarity; in (*b*), the TKE profiles are offset by 0.05.

The effect of the Reynolds number on the dynamics of the wake/boundary-layer interaction is further illustrated in figures 16 and 17. Figure 16 shows the mean velocity and turbulent kinetic energy profiles at several x-locations for the three Re_D cases. Figure 17 shows TKE profiles at three x-locations, the onset of transition,

https://doi.org/10.1017/S0022112005007342 Published online by Cambridge University Press

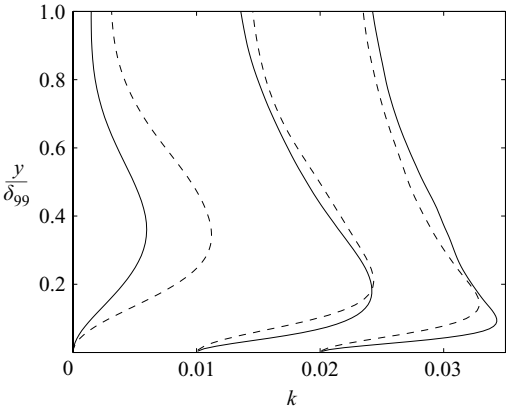


FIGURE 17. Turbulent kinetic energy profiles in the beginning, the middle and the end of the transition region; ———, $Re_D = 3900$; – – –, $Re_D = 1155$; from left to right, the streamwise locations of the profiles are $x = 30$, 50, 70 for the $Re_D = 1155$ case, and $x = 20$, 30, 40 for the $Re_D = 3900$ case.

the middle of the C_f rise ('halfway' through transition), and the onset of full-blown turbulence (the end of transition and the location of maximum C_f). The distance to the wall is normalized by the boundary-layer thickness, δ_{99} (which was computed on the basis of U_{edge} instead of U_∞, as explained in § 4.1).

The weak dependence of wake development on the Reynolds number is evident in figure 16. Apart from the initial decay of TKE in the near wake, we see relatively little difference between the profiles, despite a factor of 10 in the Reynolds numbers. We note that, because of the difference in the boundary-layer growth-rates, the turbulence intensity at the edge of the boundary layer is different for the three cases. At the beginning of the transition region, for instance, the turbulence level at the boundary-layer edge is higher by almost a factor of two in the $Re_D = 1155$ case compared to the $Re_D = 3900$ case (figure 17). It is not clear whether this difference plays a significant role in accelerating transition since the wake introduces instabilities into the boundary layer as close upstream as $x = 10$ in some instances. It is possible that increased turbulence at the edge of the boundary layer accelerates the breakdown of boundary-layer streaks. Figure 17 shows that the effect of the boundary-layer Reynolds number becomes evident after the onset of transition: the turbulent kinetic energy grows much faster in the high-Re case, and, by the end of the transition region, the turbulent kinetic energy inside the boundary layer has reached higher values than for the $Re_D = 1155$ case.

Thus, it would appear that wake-induced boundary-layer transition in the present configuration depends both on the physical distance from the plate leading edge, x/D, and on the plate Reynolds number, Re_x. The former dependence appears as an 'interaction distance', the physical streamwise distance required for the wake disturbance to contaminate the boundary layer, while the Re_x-dependence enters through the degree of boundary-layer instability, which increases with Re_x. From the above observations, we conjecture that transition may depend on a Reynolds number based on the distance from the impingement point, x_i. If, in the present simulations, we take the impingement distance to be $x_i/D = 15$, which corresponds to the streamwise location at which laminar streaks are first clearly observed, independent of Re_D (see figure 12 and the accompanying discussion), we can compute a modified Reynolds

https://doi.org/10.1017/S0022112005007342 Published online by Cambridge University Press

number as $Re_i = (x - x_i)U_\infty/\nu$. This formula yields $Re_i \simeq 17\,500$ and $Re_i \simeq 19\,500$ for the locations of transition onset at $Re_D = 1155$ and $Re_D = 3900$, respectively. In order to verify this conjecture, experiments and simulations should be carried out at higher Reynolds numbers and with varying locations of the cylinder inside the flow domain.

5. Conclusion

High-resolution DNS and LES studies of cylinder-wake-induced boundary-layer transition were carried out at three Reynolds numbers, $Re_D = 385$, 1155 and 3900. In all three cases, coherent, almost two-dimensional spanwise rollers, are present directly behind the cylinder. A short distance downstream of the cylinder, these rollers develop spanwise-periodic deformations, which cause the injection of external wake momentum into the boundary layer. The disturbances entering the boundary layer evolve into streaks of streamwise velocity, which, in the higher two Re_D cases, lead to transition to turbulence. The onset of transition occurs at relatively low Reynolds numbers, $Re_x \simeq 60\,000$ for the $Re_D = 1155$ case, and $Re_x \simeq 120\,000$ for the $Re_D = 3900$ case. The transition scenario is somewhat similar to bypass transition caused by free-stream turbulence, in which transition onset also occurs at comparable Re_x values: profiles of u_{rms} inside the perturbed laminar boundary layer were similar to those documented by Matsubara & Alfredsson (2001), and spectra of streamwise velocity showed rapid initial growth in the low-frequency component, consistent with observations of bypass transition due to f.s.t. Furthermore, for the $Re_D = 3900$ case, the transitional region was intermittent and bore similarity to intermittency in transition due to f.s.t., that is caused by the evolution of turbulent spots. Despite these similarities, the two transition scenarios are distinct in the nature of the external perturbation: in our case, it is strongly coherent and anisotropic, whereas in transition due to f.s.t., it is approximately isotropic and has no large-scale unsteadiness. One implication is that the spacing of laminar boundary-layer streaks is the same for the three cases; it is determined by the scale of the deformation of the primary roller core, which has a weak Reynolds-number dependence. In contrast, in transition due to f.s.t., laminar streaks are of the order of δ_{99} apart. For these reasons, the parallels between the two cases should be made with caution. We have examined mean velocity statistics, Reynolds stress profiles, and TKE budgets throughout the computational domain and concluded that, in the $Re_D = 1155$ and $Re_D = 3900$ cases, the boundary-layer turbulence is fully developed. Finally, we noted that in the two higher Re_D cases, transition was observed at widely different Re_x values. This phenomenon can be explained by conjecturing that transition can occur only after a fixed, nearly Re_D-independent 'impingement length', i.e. the streamwise distance required for the wake disturbance to reach the boundary layer. Once the boundary layer is contaminated, transition becomes dependent on the boundary-layer Reynolds number, Re_x. Future work will include studies of transition due to different types of upstream disturbance, such as wakes behind other types of bluff bodies.

V. O. and U. P. acknowledge the financial support of the NASA Langley Research Center, under Cooperative Agreement NAG12285.

REFERENCES

Balaras, E. 2004 Modeling complex boundaries using an external force field on Cartesian grids in large-eddy simulations. *Comput. Fluids* **33**, 375–404.

https://doi.org/10.1017/S0022112005007342 Published online by Cambridge University Press

Balaras, E., Benocci, C. & Piomelli, U. 1995 Finite difference computations of high Reynolds number flows using the dynamic subgrid-scale model. *Theoret. Comput. Fluid Dyn.* **7**, 207–216.

Balaras, E., Piomelli, U. & Wallace, J. M. 2001 Self-similar states in turbulent mixing layers. *J. Fluid Mech.* **446**, 1–24.

Bandyopadhyay, P. R. 1987 Resonant flow in a row of small transverse cavities submerged in a turbulent boundary layer. *AIAA Paper* 1987-1235.

Brandt, L., Schlatter, P. & Henningson, D. S. 2004 Transition in boundary layers subject to free-stream turbulence. *J. Fluid Mech.* **517**, 167–198.

Chorin, A. J. 1968 Numerical solution of the Navier–Stokes equations. *Maths Comput.* **22**, 742–762.

Fadlun, E. A., Verzicco, R., Orlandi, P. & Mohd-Yusof, J. 2000 Combined immersed-boundary finite-difference methods for three-dimensional complex flow simulations. *J. Comput. Phys.* **161**, 35–60.

Henningson, D., Spalart, P. & Kim, J. 1987 Numerical simulations of turbulent spots in plane Poisseuille and boundary-layer flow. *Phys. Fluids* **30**, 2914–2917.

Huai, X., Joslin, R. D. & Piomelli, U. 1997 Large-eddy simulation of transition to turbulence in boundary layers. *Theoret. Comput. Fluid Dyn.* **9**, 149–163.

Jacobs, G. J. & Durbin, P. A. 2001 Simulations of bypass transition. *J. Fluid Mech.* **428**, 185–212.

Kim, J. & Moin, P. 1985 Application of a fractional step method to incompressible Navier–Stokes equations. *J. Comput. Phys.* **59**, 308–323.

Klebanoff, P. S. 1971 Effect of freestream turbulence on the laminar boundary layer. *Bull. Am. Phys. Soc.* **10**, 1323.

Kravchenko, A. G. & Moin, P. 2000 Numerical studies of flow over a circular cylinder at $Re_D = 3900$. *Phys. Fluids* **12**, 403–417.

Kusunose, K. & Cao, H. V. 1994 Prediction of transition location for a 2-D Navier–Stokes solver for multi-element airfoil configurations. *AIAA Paper* 1994-2376.

Kyriakides, N. K., Kastrinakis, E. G., Nychas, S. G. & Goulas, A. 1996 Boundary layer transition induced by a von Kármán vortex street wake. *Proc. Instn. Mech. Engrs* **210**, 167–179.

Kyriakides, N. K., Kastrinakis, E. G., Nychas, S. G. & Goulas, A. 1999 A bypass wake-induced laminar turbulent transition. *Eur J. Mech.* B/*Fluids* **18**, 1049–1065.

Liu, X. & Rodi, W. 1991 Experiments on transitional boundary layers with wake-induced unsteadiness. *J. Fluid Mech.* **231**, 229–256.

Matsubara, M. & Alfredsson, H. 2001 Disturbance growth in boundary layers subjected to free-stream turbulence. *J. Fluid. Mech.* **430**, 149–168.

Meneveau, C., Lund, T. S. & Cabot, W. H. 1996. A Lagrangian dynamic subgrid-scale model of turbulence. *J. Fluid Mech.* **319**, 353–385.

Meredith, P. T. 1993 Viscous phenomena affecting high-lift systems and suggestions for future CFD development. *AGARD CP*515, pp. 19.1–19.8.

Morinishi, Y., Lund, T. S., Vasilyev, O. V. & Moin, P. 1998 Fully-conservative higher order finite difference schemes for incompressible flow. *J. Comput. Phys.* **143**, 90–124.

Moser, R. D., Kim, J. & Mansour, N. N. 1999 Direct numerical simulation of turbulent channel flow up to $Re_\tau = 500$. *Phys. Fluids* **11**, 943–945.

Ong, L. & Wallace, J. 1996 The velocity field of the turbulent very near wake of a circular cylinder. *Exps. Fluids* **20**, 441–453.

Orlanski, I. 1976 Simple boundary condition for unbounded hyperbolic flows. *J. Comput. Phys.* **21**, 251–269.

Ovchinnikov, V. O., Piomelli, U. & Choudhari, M. M. 2004 Inflow conditions for numerical simulations of bypass transition. *AIAA Paper* 2004-0591.

Piomelli, U., Balaras, E. & Pascarelli, A. 2000 Turbulent structures in accelerating boundary layers. *J. Turbulence* **1**, 1–16.

Piomelli, U., Choudhari, M. M., Ovchinnikov, V. O. & Balaras, E. 2004 Numerical simulations of wake/boundary layer interactions. *AIAA Paper* 2004-0975.

Rai, M. M. & Moin, P. 1993 Direct numerical simulation of transition and turbulence in a spacially evolving boundary layer. *J. Comput. Phys.* **109**, 169–192.

Roach, P. E. & Brierley, D. H. 1992 The influence of a turbulent free-stream on zero pressure gradient transitional boundary layer development. Part I: test cases T3A and T3B.

https://doi.org/10.1017/S0022112005007342 Published online by Cambridge University Press

In *Numerical Simulation of unsteady flows and transition to turbulence* (ed. O. Pironneau, W. Rodi, I. L. Rhyming, A. M. Savill & T. V. Truong), pp. 319–347. Cambridge University Press.

Spalart, P. R. 1986 Numerical study of sink flow boundary layers. *J. Fluid Mech.* **172**, 307–328.

Squire, L. C. 1989 Interactions between wakes and boundary-layers. *Prog. Aerospace Sci.* **26**, 261–288.

Westin, K. J. A., Boiko, B. G. B., Klingmann, G. B., Kozlov, V. V. & Alfredsson, P. H. 1994 Experiments in a boundary layer subjected to free stream turbulence. Part 1. Boundary layer structure and receptivity. *J. Fluid. Mech.* **281**, 193–218.

Williamson, C. H. K. 1996 Three-dimensional wake transition. *J. Fluid Mech.* **328**, 345–407.

Wu, X., Jacobs, R. G., Hunt, J. C. R. & Durbin, P. A. 1999 Simulation of boundary layer transition induced by periodically passing wakes. *J. Fluid Mech.* **398**, 109–153.

Zhou, M. D. & Squire, L. C. 1985 The interaction of a wake with a turbulent boundary-layer. *J. Aeronaut.* **89**, 72–81.

https://doi.org/10.1017/S0022112005007342 Published online by Cambridge University Press